JOURNAL OF SOLID STATE CHEMISTRY **134,** 395–408 (1997)
ARTICLE NO. SC977612

A New Manganese Oxyborate, $Sr_4Mn_3(B_{1-x}Mn_x)O_{10}$, Closely Related to the Perovskite Structure Type

D. Pelloquin, M. Hervieu, C. Michel, N. Nguyen, and B. Raveau

Laboratoire CRISMAT, ISMRA et Université de Caen, UMR 6508 associée au CNRS, Bd. du Maréchal Juin, 14050 Caen Cedex, France

Received March 7, 1997; in revised form September 4, 1997; accepted September 5, 1997

A new strontium manganese oxyborate $Sr_4Mn_{3+x}B_{1-x}O_{10}$, related to the cubic perovskite structure, was synthesized by solid-state reaction. It crystallizes in an orthorhombic cell with the *Amm*2 space group. The cell parameters are related to a cubic perovskite cell (a_p) by $a=a_p=3.7865(1)$ Å, $b=4a_p=15.8540(4)$ Å, and $c=2a_p=7.6540(1)$ Å. The structural study shows that this oxyborate with ideal formula $Sr_4Mn_3BO_{10}$, derived from the perovskite $SrMnO_3$, consists of a deficient perovskite matrix $Sr_4Mn_3O_8$ built by corner-sharing MnO_5 pyramids. This framework forms large tunnels parallel to the [100] direction occupied by triangular BO_3 groups. A HREM study, coupled with EDX and XRD analyses, shows that the actual composition is close to $Sr_4Mn_{3.2}B_{0.8}O_{10}$ involving the presence of complex structural phenomena. This compound is antiferromagnetic with a Neel temperature $T_N \approx 240$ K.

INTRODUCTION

The great flexibility of the perovskite structure type has allowed generation of materials with specific physical properties. In these oxides, the perovskite framework plays the role of a host matrix for various anionic species. This is, for instance, the case for copper oxycarbonates which exhibit superconducting properties up to 110 K (for review, see refs. 1 and 2), where the triangular carbonate groups are sandwiched between octahedral or pyramidal perovskite-like layers. The triangular borate groups can also be accommodated by the perovskite structure type, owing to their very similar geometry and size to that of the carbonate group. The synthesis of the layered oxyborates $LnBaCuBO_3O_2$ (3), closely related to the oxycarbonates, confirms this point of view.

The realization of such mixed frameworks, built of CuO_6 octahedra and BO_3 or CO_3 triangular groups, is in fact possible because of the Jahn–Teller effect of Cu^{2+}. This produces more flexible apical Cu–O bonds of the CuO_6 octahedra, which compensate the great rigidity of the triangular borate or carbonate groups. Owing to its d^4 electronic configuration, Mn(III) exhibits also a Jahn–Teller distortion, so that distorted MnO_6 octahedra and MnO_5 pyramids can be formed. Therefore, trivalent manganese is a good candidate for the formation of a mixed framework involving CO_3 or BO_3 groups. This viewpoint is supported by the synthesis of the oxycarbonate $Sr_5Mn_4CO_3O_{10}$ (4). The latter is also closely related to perovskite, but it consists of a $[Mn_4O_{10}]_\infty$ framework built of MnO_5 pyramids, forming tunnels where the carbonate groups are located.

From the foregoing considerations, it appears that Mn(III) oxyborates should exist. For this reason, we have investigated the system Sr–B–Mn(III)–O. In the present study, we describe the structure and magnetic properties of a new Mn(III) oxyborate, $Sr_4Mn_{3+x}B_{1-x}O_{10}$, whose three-dimensional host lattice $[Mn_3O_8]_\infty$, built of MnO_5 pyramids, is also derived from the perovskite structure type, forming tunnels parallel to [100] where the BO_3 groups are located.

EXPERIMENTAL PROCEDURE

The system Sr–Mn–B–O was investigated, starting from various mixtures of SrO, Mn_2O_3, and B_2O_3, according to the theoretical cation ratio "$SrMn_{1-x}B_x$." To avoid carbonate contamination, SrO was initially prepared by decomposing SrO_2 or $Sr(OH)_2 \cdot 6H_2O$ and stored in a drybox. The precursors were weighed according to the cationic composition chosen, intimately ground in an agate mortar, and placed in an alumina finger. This step was performed in a drybox. Each mixture was sealed in an evacuated silica ampule, heated to 1000°C at 150°C h^{-1}, kept at this temperature for 24 h, and cooled to room temperature at 150°C h^{-1}.

The electron diffraction (ED) study was carried out using a JEOL 200 CX electron microscope fitted with a eucentric goniometer ($\pm 60°$) and equipped with an EDX analyzer. High-resolution electron microscopy (HREM) was performed with a TOPCON 002B operating at 200 kV and having a point resolution of 1.8 Å. HREM image calculations were carried out with the Mac-Tempas multislice program.

0022-4596/97 $25.00

The structural model was refined from powder X-ray diffraction (XRD) data collected at room temperature, with a Philips vertical diffractometer (Cu$K\alpha$ radiation) equipped with a secondary graphite monochromator and a proportional detector, in the range $6^\circ \leq 2\theta \leq 110^\circ$ in increments of 0.02° (2θ) using the program Fullprof (version 3.1d) (5). A pseudo-Voigt function was used for peak shape calculations and the background was subtracted from a linear interpolation between experimental points.

The susceptibility measurements were made between 100 and 600 K with the Faraday method in an applied field of about 300 G.

RESULTS

Following the experimental procedure, a new black phase was isolated from nominal compositions close to $Sr_4Mn_3BO_{10}$. In fact, the EDX analysis performed on numerous crystallites showed the systematic existence of a small manganese excess with respect to the ideal cationic composition $Sr:Mn:B = 4:3:1$, leading to an actual composition $Sr_4Mn_{3+x}B_{1-x}O_{10}$ with $x \approx 0.2$.

X-Ray Diffraction and HREM Study

The reconstruction of the reciprocal space, using electron diffraction, allows an orthorhombic cell closely related to a perovskite subcell (a_p) to be evidenced with $a \approx a_p$, $b \approx 4a_p$, and $c \approx 2a_p$. The conditions limiting the reflections are hkl, $k + l = 2n$, compatible with the space groups $Ammm$, $A2mm$, $Amm2$, and $A222$. This is illustrated by the [100] and [001] ED patterns displayed in Figs. 1a and 1b, respectively. The systematic existence of 90° oriented domains is a common feature, as usually observed in perovskite-related materials which exhibit superstructures resulting from long-range ordering or framework distortions. It results from the fact that the superstructure takes place along one of the three equivalent $[100]_p$ orientations of the cubic perovskite subcell. Extra reflections lying in incommensurate positions are sometimes observed along a^*. These features will be detailed later. On the basis of these observations, the powder XRD pattern can be indexed in an orthorhombic cell with $a = 3.7865(1)$ Å, $b = 15.8540(4)$ Å, and $c = 7.6540(1)$ Å.

Taking into consideration the ideal formula $Sr_4Mn_3BO_{10}$ and the fact that this structure derives from the ideal ABO_3 perovskite, an ordered replacement of Mn polyhedra by triangular BO_3 groups can be proposed. Such an ordering of the Mn and B species should be easily identified by high-resolution electron microscopy; it has been shown indeed to give rise to typical modifications of the contrast for copper oxycarbonates and oxynitrates (1, 2) and for manganese oxycarbonate (4). The [100] HREM images (Fig. 2a) confirm this viewpoint: small crosses of very bright dots are observed in the thin parts of the crystallites, which are correlated to the positions of the borate groups (boron atom surrounded by oxygens and vacancies), whereas in the thicker areas only bright dots are observed. These groups are $2a_p$ spaced along $\vec{c}$ and $4a_p$ spaced along $\vec{b}$ and the image is centered, in agreement with the A-type symmetry. From these observations, a model can be proposed for the cationic arrangement of this phase (Fig. 2b) for which the strontium cations occupy the same positions as in the ideal perovskite structure, whereas the ordering between B and Mn derives from that observed in the perovskite in the following way:

(i) one (010) layer out of two Mn polyhedra is untouched;

(ii) in the second (010) layer, one [100] manganese row out of two is replaced by a boron row along $\vec{c}$, forming mixed but ordered "MnB" (010) layers;

(iii) two successive (010) mixed "MnB" layers are shifted by $\vec{c}/2$ with respect to each other, leading to a quadrupling of the a_p parameter along $\vec{b}$.

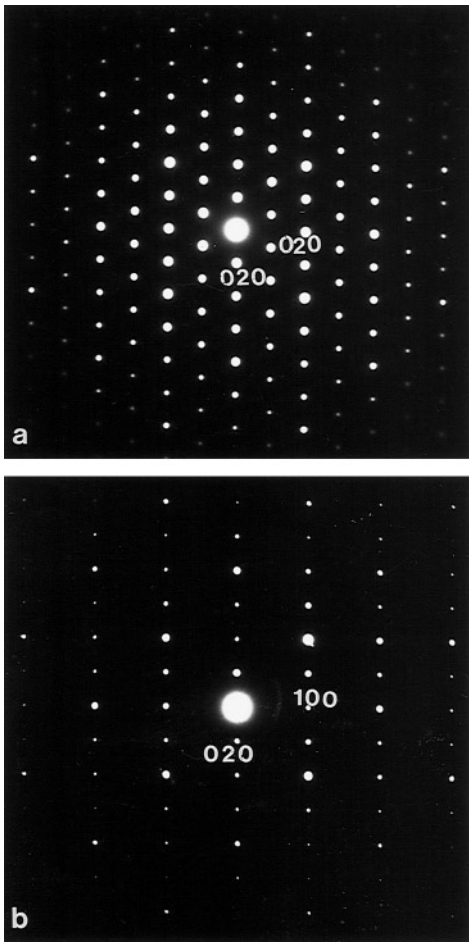

FIG. 1. (a) [100] and (b) [001] ED patterns, illustrating the conditions limiting the reflections: hkl, $k + l = 2n$.

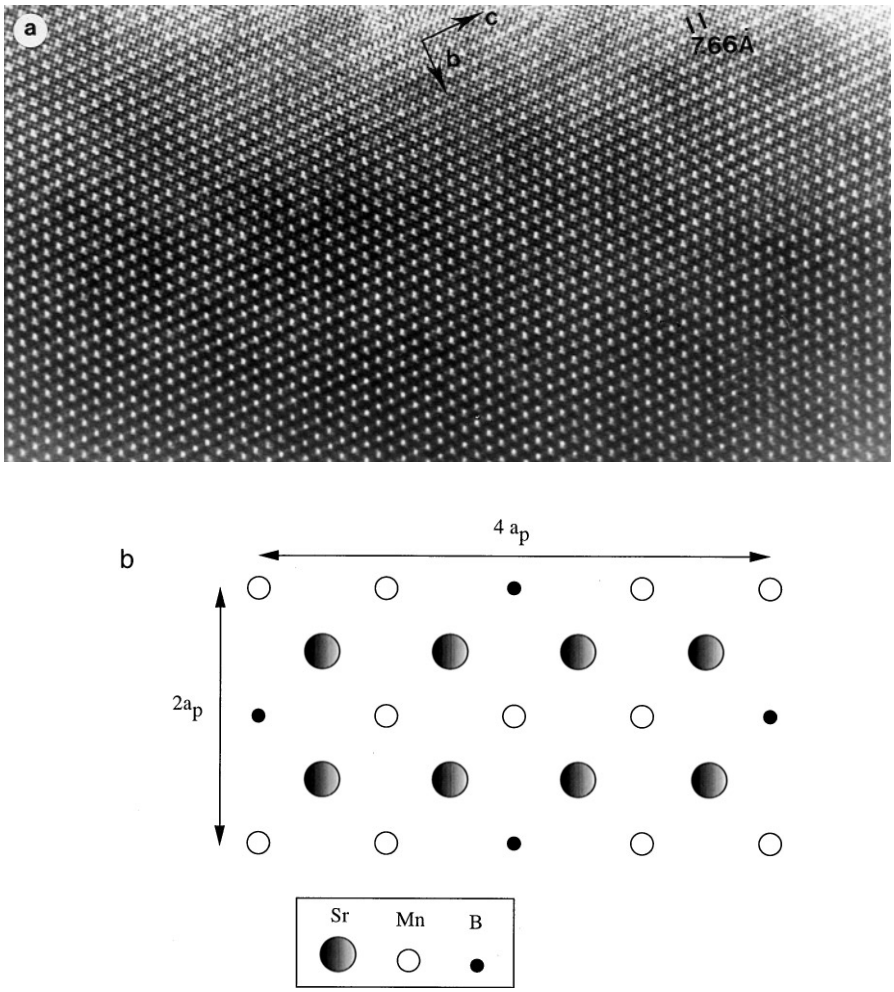

FIG. 2. (a) Typical [100] HREM image; the small bright dots are correlated to the positions of the borate groups. (b) The arrangement of the cation positions, as deduced from the image, is schematically drawn.

This cationic arrangement, which corresponds to the ideal composition "Sr_4Mn_3B," was first considered for the determination of the structure from powder X-ray data. The origin of the cell was chosen on a manganese. Whatever the considered space group—*Ammm*, *A*2*mm*, *Amm*2, or *A*222—the refined parameters of the cationic positions are almost identical. At this stage, successive Fourier difference map sections were undertaken to locate the oxygen atoms. They were carried out in the less symmetric space group *Amm*2 to avoid the artificial generation of Fourier peaks, considering particular values for the positional variable x (0 or $\frac{1}{2}$) induced by the perovskite framework. Successive Fourier difference maps evidence identical layers of cornersharing MnO_5 pyramids parallel to (010). The corresponding oxygen positions (from O(1) to O(4)) and the cation positions were then refined, leading to the agreement factor based on intensities $R_i = 0.165$. For this refinement and the next ones, Mn(2), which is twice Mn(1), was fixed at (0, 0.25, 0) to determine more accurately the cell origin. At this stage, a Fourier difference section at $x = 0$, the level of the assumed boron position (0, $\frac{1}{2}$, 0), allowed observation of three residues at a distance close to 1.4 Å (Fig. 3), which could be attributed to the oxygens forming the borate groups. Boron

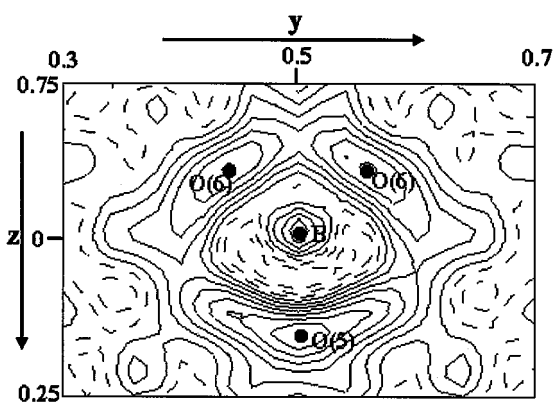

FIG. 3. Fourier difference section at $x = 0$.

TABLE 1
Structural Data Obtained after Refinement in the Space Group *Amm*2

Atom	Site	x	y	z	B_{iso} (Å^2)	t	Interatomic distances (Å) and angles (deg)	
Mn(1)	2*a*	0	0	0.0078(36)	0.5(3)	1	Mn(1)–O(1) × 2	1.894(1)
Mn(2)	4*d*	0	0.25	0	0.1(2)	1	Mn(1)–O(2) × 2	1.92(2)
B	2*a*	0	0	0.5[a]	1	1	Mn(1)–O(5) × 1	2.47(4)
Sr(1)	4*e*	$\frac{1}{2}$	0.3665(3)	0.2538(22)	0.1(1)	1	Mn(2)–O(3) × 2	1.912(3)
Sr(2)	4*e*	$\frac{1}{2}$	0.1263(3?)	0.2284(24)	0.8(1)	1	Mn(2)–O(4) × 2	1.913(1)
O(1)	2*b*	$\frac{1}{2}$	0	0[a]	1	1	Mn(2)–O(2) × 1	2.04(2)
O(2)	4*d*	0	0.1211(16)	0[a]	1	1	Mn(2)–O(6) × 1	2.84(2)
O(3)	4*e*	$\frac{1}{2}$	0.2669(15)	0[a]	1	1		
O(4)	4*d*	0	0.25[a]	0.25[a]	1	1	Sr(1)–O(1) × 1	2.84(1)
O(5)	2*a*	0	0	0.3159(47)	1	1	Sr(1)–O(2) × 2	2.68(1)
O(6)	4*d*	0	0.4243(15)	− 0.0882(32)	1	1	Sr(1)–O(3) × 1	2.50(2)
							Sr(1)–O(3) × 1	2.83(2)
							Sr(1)–O(4) × 2	2.645(3)
							Sr(1)–O(5) × 2	2.889(8)
							Sr(2)–O(1) × 1	2.66(1)
							Sr(2)–O(2) × 2	2.58(1)
							Sr(2)–O(3) × 1	2.83(2)
							Sr(2)–O(3) × 1	2.68(2)
							Sr(2)–O(4) × 2	2.731(4)
							Sr(2)–O(6) × 2	2.49(2)
							B–O(6) × 2	1.38(2)
							B–O(5) × 1	1.41(3)
							O(5)–B–O(6)	121(1)
							O(6)–B–O(5)	119(1)

Space group: *Amm*2 (No. 38)
$a = 3.7865(1)$ Å
$b = 15.8540(4)$ Å
$c = 7.6540(2)$ Å
$\chi^2 = 6.04$
$R_i = 0.076$

[a] Variable not refined in the final calculations because e.s.d.'s value is larger than the displacement.

and surrounding oxygen atoms—O(5) at (0, $\frac{1}{2}$, 0.18) (2*a* site) and O(6) at (0, 0.44, 0.88) (4*d* site)—were then introduced into the calculations. Refinement of all positional parameters and the isotropic *B* factors for strontium and manganese atoms (*B* factors for oxygens and boron being fixed at 1 Å^2) decreased the R_i factor to 0.08 ($R_i = 0.076$, $\chi^2 = 6.04$) (Table 1). Observed, calculated, and final difference patterns are plotted in Fig. 4. Calculations were also performed keeping the same cell parameters ($a_p \times 4a_p \times 2a_p$) in the space group *Am*2*m*, which allows a 90° rotation of the BO_3 groups in the (100) plane. They lead to similar *R* values for the positional parameters given in Table 2. Thus it is not possible to determine the right orientation of the BO_3 groups from X-ray diffraction. Nevertheless, the first hypothesis (*Amm*2) that leads to MnO_5 pyramids with correct Mn(1)–O distances (1.9–2.47 Å) is more likely than the second one (*Am*2*m*) that generates elongated MnO_6 octahedra with abnormally long Mn(1)–O apical bonds (2.72 Å).

Simulated HREM images were calculated for each of these two models (Tables 1 and 2), varying the focus values and the crystal thickness, and then they were compared to the experimental ones. From the simulations, one observes that only a few images allow the two models to be differentiated, for a given crystal thickness, due to the very close positional parameters. The [100] through-focus series calculated for a crystal thickness of 20 Å are given as examples in Figs. 5a and 5b for models "*Am*2*m*" and "*Amm*2," respectively (boron positions are indicated by white triangles in the −550 Å images and enlarged structure projections are displayed below, where the borate groups are drawn as black triangles). The difference in contrast is generated by the orientation of the borate groups and the surrounding oxygen atoms, leading to asymmetric images with regard to the (001) and (010) planes, in agreement with the different positions of the mirrors *m*. This difference is clearly visible with increasing crystal thickness. This is illustrated in Fig. 6, calculated for crystal thicknesses ranging between 12 and 75 Å. For a focus value close to −300 Å (Fig. 6a), the light electron density zones appear as white dots and the boron positions as gray dots (white triangles). The image is symmetric with regard to (001) in model "*Am*2*m*" and with regard to (010) in model "*Amm*2." This is observed at the level of the small white crosses (oxygens and vacancies around the B position), for which the four dots are not of equal intensity: the modulation of intensity is observed

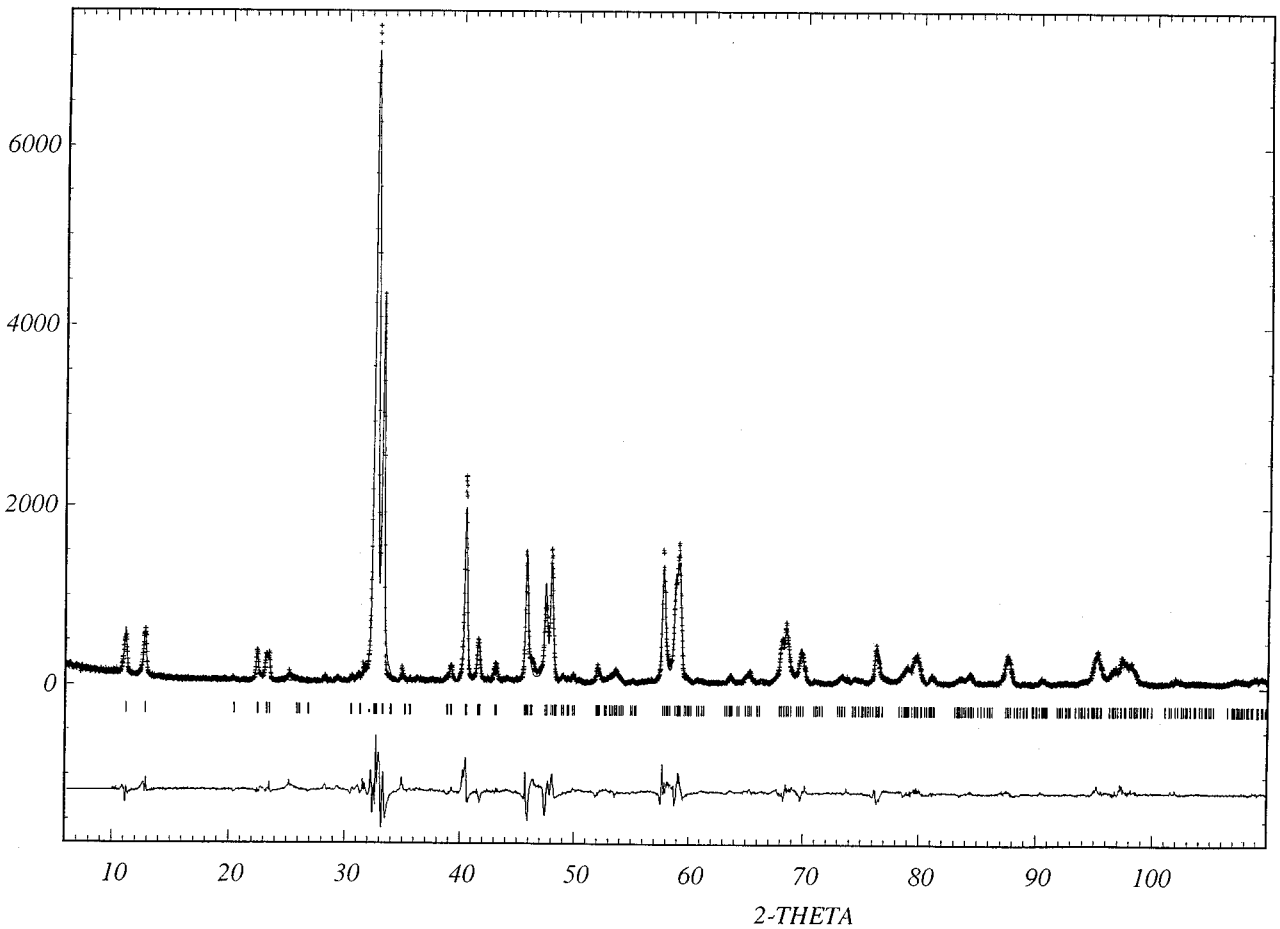

FIG. 4. Experimental (crosses), calculated, and difference (solid lines) X-ray diffraction patterns for $Sr_4Mn_3BO_{10}$.

along $\vec{b}$ for model "*Am*2*m*" and along $\vec{c}$ for model "*Amm*2." For a focus value close to -600 Å, the heavy atoms (Sr and Mn) are imaged as bright dots and boron as gray dots (small white triangles) and the modulation of intensity is indeed observed along the same directions. The corresponding experimental images are given in Figs. 7a and 7b, assumed to correspond to focus values of -300 and -600 Å, respectively. The asymmetry of these images suggests that the mirror plane is (010) in the major part of the crystal, so model "*Amm*2" is most probable.

Note that modulations of intensity are observed at the level of and around the boron positions, which are assumed to be associated with local variations of stoichiometry around this position. This observation is in agreement with the EDX analysis, which evidences a manganese excess with respect to the ideal formula.

At this point, Fourier difference synthesis, performed for the model "*Amm*2," showed a residual on the boron sites, suggesting that a part of these positions may be occupied by manganese. Refinements of the occupancy factors of the boron sites confirm this viewpoint, leading to the presence of 20% Mn on the B sites, in agreement with the formula $Sr_4Mn_{3.2}B_{0.8}O_{10}$. In this way, the reliability factors were indeed significantly lowered to $\chi^2 = 5.7$ and $R_i = 0.065$. This partial replacement of boron by manganese implies also a variation of the oxygen distribution around the B site; the latter cannot be detected, of course, from powder X-ray data but is suggested by HREM observations as stated earlier.

Description of the Structure

This structural study confirms that the structure of the oxyborate with ideal formula $Sr_4Mn_3BO_{10}$ is closely related to the "ideal cubic" perovskite ABO_3. As shown from the projection of the structure along $\vec{a}$ (Fig. 8), it consists of a deficient perovskite matrix $Sr_4Mn_3O_8$, built up from corner-sharing MnO_5 pyramids; the latter derives from the stoichiometric perovskite by removing one [100] row of MnO_6 octahedra out of four in an ordered way. This results

TABLE 2
Structural Data Obtained after Refinement in the Space Group *Am2m*

Atom	Site	x	y	z	B_{iso} (Å^2)	t	Interatomic distances (Å) and angles (deg)	
Mn(1)	2*a*	0	− 0.009(4)	0	0.3(3)	1	Mn(1)–O(1) × 2	1.899(5)
Mn(2)	2*a*	0	0.25	0	0.3(3)	1	Mn(1)–O(3) × 1	2.12(5)
Mn(3)	2*a*	0	0.75	0	0.2(3)		Mn(1)–O(6) × 2	2.72(3)
B	2*a*	0	0.5[a]	0	1	1	Mn(1)–O(3′) × 1	1.84(5)
Sr(1)	4*e*	$\frac{1}{2}$	0.3763(40)	0.2504(8)	0.5(2)	1	Mn(2)–O(2) × 2	1.94(2)
Sr(2)	4*e*	$\frac{1}{2}$	0.1343(38)	0.2287(5)	0.2(2)	1	Mn(2)–O(3) × 1	2.06(5)
O(1)	2*b*	$\frac{1}{2}$	0[a]	0	1	1	Mn(2)–O(4) × 2	1.914(4)
O(2)	2*b*	$\frac{1}{2}$	0.2816(50)	0	1	1	Mn(2)–O(5) × 1	2.37(5)
O(2′)	2*b*	$\frac{1}{2}$	0.7453(57)	0	1	1		
O(3)	2*a*	0	0.1247(55)	0	1	1	Mn(3)–O(2′) × 2	1.900(9)
O(3′)	2*a*	0	0.8750(52)	0	1	1	Mn(3)–O(3′) × 1	1.90(5)
O(4)	4*d*	0	0.25[a]	0.25[a]	1	1	Mn(3)–O(4) × 2	1.914(3)
O(5)	2*a*	0	0.4044(47)	0	1	1		
O(6)	4*d*	0	0.5322(41)	− 0.1544(27)	1	1	Sr(1)–O(1) × 1	2.74(4)
							Sr(1)–O(2) × 1	2.43(6)
							Sr(1)–O(2′) × 1	2.82(8)
							Sr(1)–O(3′) × 2	2.690(4)
							Sr(1)–O(4) × 2	2.66(8)
							Sr(1)–O(5) × 2	2.73(2)
							Sr(2)–O(1) × 1	2.76(5)
							Sr(2)–O(2) × 1	2.92(8)
							Sr(2)–O(2′) × 1	2.72(7)
							Sr(2)–O(3) × 2	2.583(7)
							Sr(2)–O(4) × 2	2.74(8)
							Sr(2)–O(6) × 2	2.65(5)
							B–O(6) × 2	1.29(3)
							B–O(5) × 1	1.51(7)
							O(6)–B–O(6)	133(3)
							O(6)–B–O(5)	113(2)

Space group: *Am2m* (No. 38)
$a = 3.7865(1)$ Å
$b = 15.8540(4)$ Å
$c = 7.6540(2)$ Å
$\chi^2 = 6.05$
$R_i = 0.077$

[a]Variable not refined in the final calculations because e.s.d.'s value is larger than the displacement.

in large tunnels running along $\vec{a}$ which are occupied by triangular BO_3 groups (dark triangles in Fig. 8). The BO_3 groups are equiplanar to (100) and share one apex with one MnO_5 pyramid. This structural behavior is very similar to that described for the manganese oxycarbonate $Sr_5Mn_4CO_3O_{10}$ (4). In this compound, the $[Mn_4O_{10}]_\infty$ host lattice is also derived from the ideal perovskite structure by elimination of rows of MnO_6 octahedra in an ordered way, but it differs from the oxyborate $Sr_4Mn_3BO_{10}$ by the fact that one row of octahedra out of five is removed instead of one row out of four, leading to a different shape of the tunnels. Note that the mode of connection of the BO_3 group to the MnO_5 pyramid, leaving two "free" apices for each group (outlined by the dotted lines in Fig. 8), is similar to that observed in the copper oxyborates $LnBaCuBO_3O_2$ (3).

The interatomic distances deduced from the XRD study are listed in Table 1. They show that the oxygen atoms that form the $[Mn_3O_8]_\infty$ pyramidal framework exhibit usual Mn–O distances. The pyramids are indeed formed of four equatorial Mn–O bonds ranging from 1.89 to 1.92 Å and one apical Mn–O bond ranging from 2.04 to 2.47 Å. The O atoms that form the two "free" apices of each BO_3 group (Fig. 8) are located at 2.84 Å from the Mn(2) atoms. As a consequence, strongly distorted MnO_6 octahedra are formed in a similar way as in $Sr_5Mn_4CO_3O_{10}$ (4). Thus the structure of this new oxyborate can also be described as built by layers of distorted MnO_6 octahedra parallel to (010) (dotted lines added to the projected pyramids in Fig. 8) which are interconnected through rows of BO_3 groups and MnO_5 pyramids running along [100]. Such a description shows that the ideal compound $Sr_4Mn_3BO_{10}$ is closely related to the copper oxycarbonates $Y_n(Ba,Sr)_{2n}Cu_{3n-1}CO_3O_{7n-3}$ (6, 7), whose structure consists of oxygen-deficient perovskite layers interconnected through rows of CO_3 groups and CuO_5 pyramids.

In fact, the actual structure of the present compound is more complex, since an excess of manganese has been detected by EDX analysis and confirmed by XRD refinements. The magnetic study of this phase, which is detailed later, supports also the existence of a manganese excess and

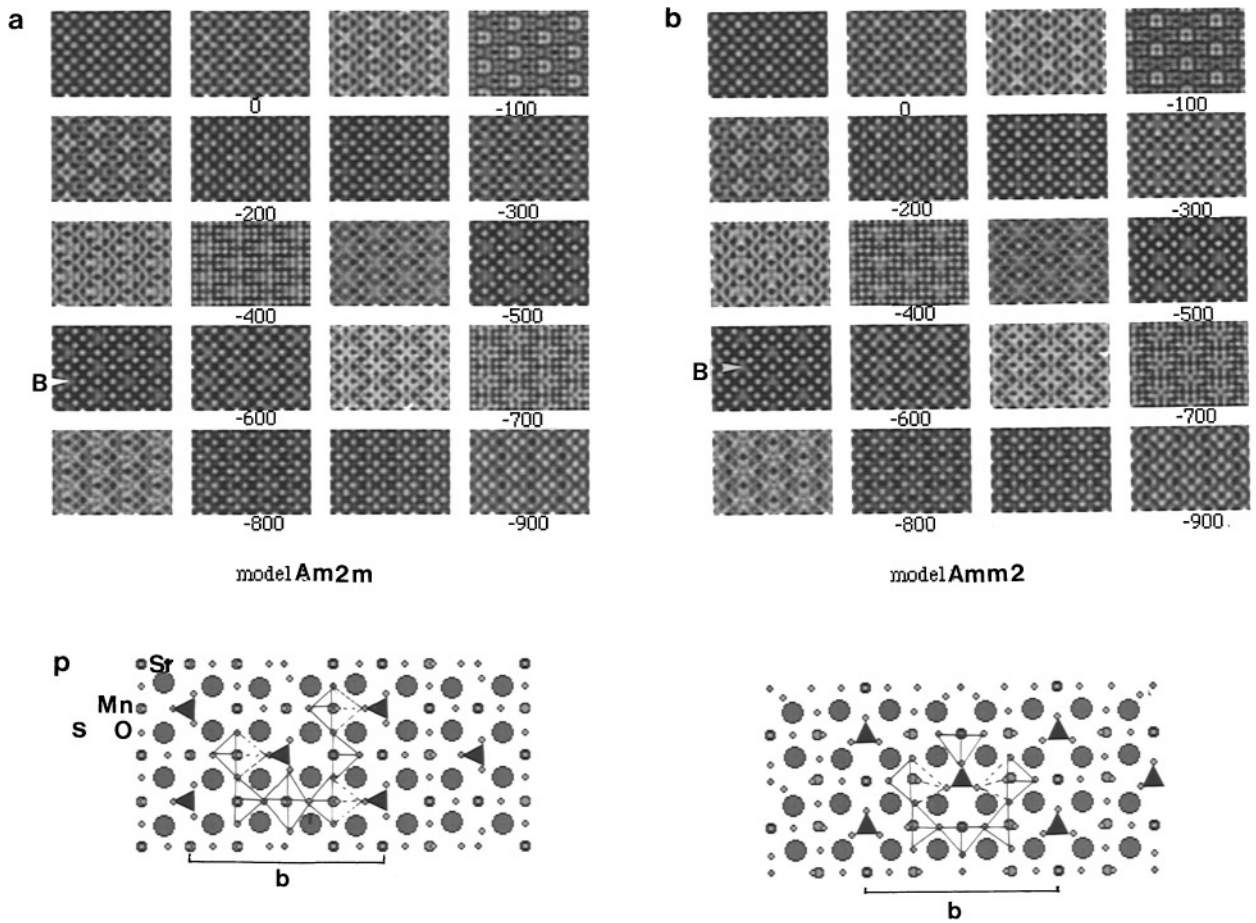

FIG. 5. Simulated through-focus series (crystal thickness ≈ 20 Å, focus values are given in angstrons), calculated for (a) the model "*Am2m*" (positional parameters in Table 2) and (b) the model "*Amm*2" (positional parameters in Table 1). The projection of the atomic positions is given for each model, where the borate groups are drawn as black triangles. In the calculated images, only the B position is indicated (white arrowhead).

implies that all the manganese should be trivalent. Consequently, the actual formula of this new phase can be written $Sr_4Mn_{3.2}B_{0.8}O_{10}$. Such a formula is easily explained by the replacement of BO_3 groups by MnO_5 pyramids in the large tunnels. The oxygen stoichiometry "O_{10}" can indeed be maintained for pure pyramidal frameworks derived from the ideal perovskite structure. This has been demonstrated for the oxygen-deficient perovskites $Ca_2Mn_2O_5$ (8) and $Sr_2Mn_2O_5$ (9).

Nanostructures

Domains. As mentioned earlier, the electron microscopy investigation, ED and HREM, shows that the formation of 90° oriented domains is a rather frequent phenomenon. An example is given in Fig. 9a, where three adjacent domains are observed.

In the right part of the image, the crystal is viewed along [100] and we see clearly the centered contrast characteristic of this orientation. In the middle part, the crystal is [001] oriented, the $\vec{b}$ axis being parallel to that of the [100] adjacent domain. The boundary between these two [100] and [001] domains is not planar. The enlarged image in Fig. 9b shows that the rows of pyramids running along $\vec{c}$, i.e., the $[MnO_2]_\infty$ layers parallel to (010), are continuous through the domain boundary (DB). On the opposite, the rows built up from one borate group alternating with one Mn pyramid are perpendicularly oriented. This is illustrated in the idealized scheme in Fig. 9c. To make the projection of the structure simpler, only a single layer is drawn, parallel to (001) and (100), depending on the domain.

In the left part of Fig. 9a, twinning domains are observed within the [001] zone of the crystallite. Contrary to the boundary parting the [001] and [100] domains, such a twin boundary is always planar and parallel to (120), i.e., to the $(110)_p$ plane of the cubic subcell. As a result of this type of twinning mechanism, the "pure" pyramidal layers are perpendicular but here again, they are connected together

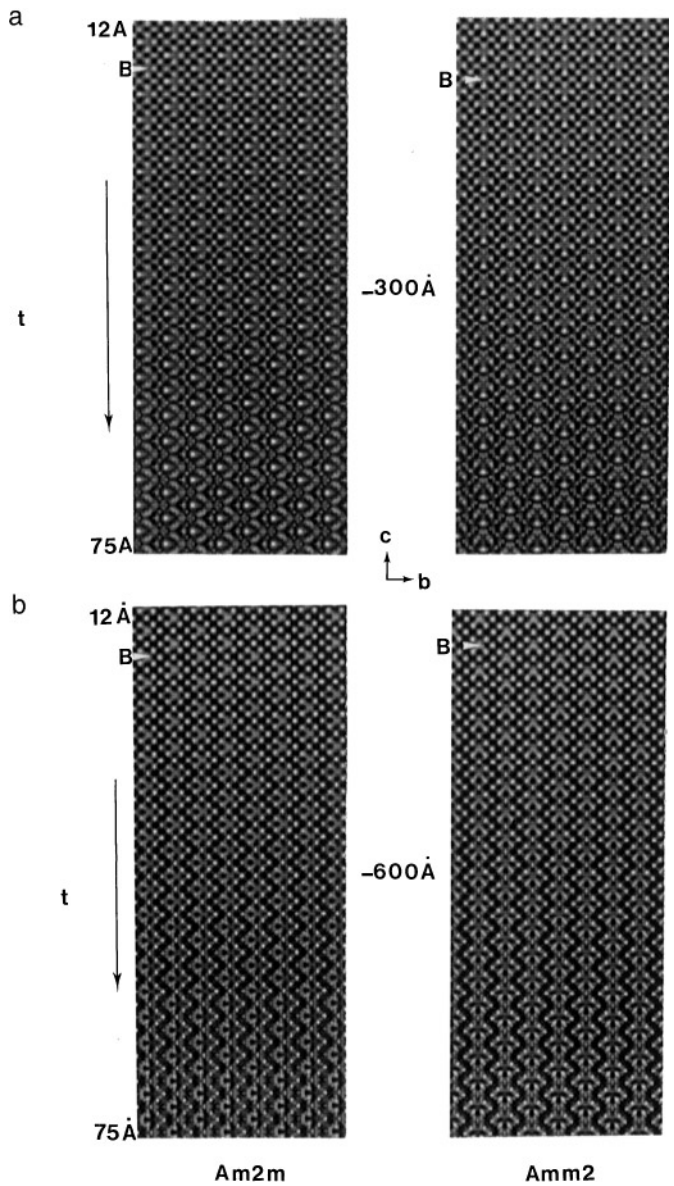

FIG. 6. Evolution of the contrast with the crystal thickness (t) from 12 to 75 Å for two characteristic focus values, −300 and −600 Å: (a) model "*Am*2*m*" and (b) model "*Amm*2."

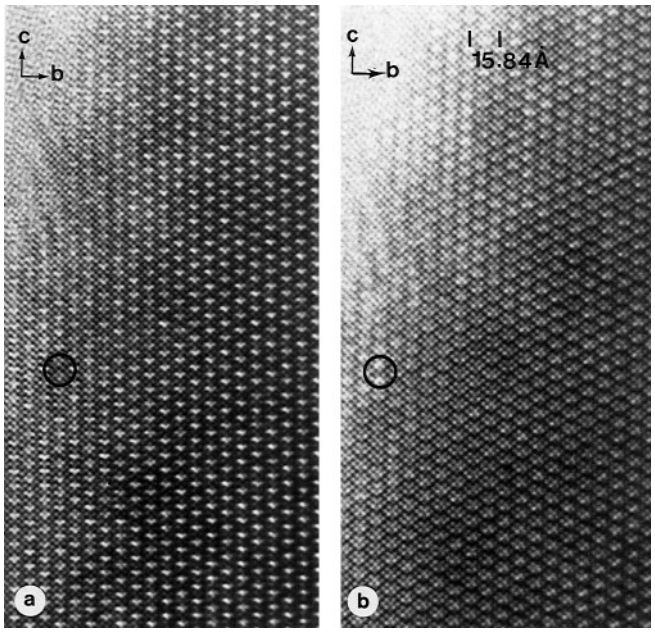

FIG. 7. Experimental [100] HREM images recorded for two focus values which are assumed to be close to (a) −300 Å and (b) −600 Å. A local variation of the contrast at the level of the boron position is observed in the circled area.

through the twin boundary. The mixed chains adopt the same configuration; i.e., they are perpendicular and are connected together.

The different nature of the boundaries, namely those parting the [100] and [001] domains (which are not planar) in contrast to the planar twin boundaries, can be easily understood. One of the important structural parameters could be the retention of the pyramidal framework through the direct connection of the $[MnO_2]_\infty$ layers parallel to (010). According to this hypothesis, the connection between [001] and [100] oriented domains could be ensured at any level of the mixed layer: the domain boundary is therefore not necessarily planar.

B and Mn distribution. (*i*) *Isolated Defects.* As already mentioned, contrast variations are observed at the level of the boron atoms and surrounding positions. The possible different orientations of the triangular borate group (*vide supra*) is a possible explanation for this variation, but another one is the nature of the cation occupying the boron site. The through-focus series show clearly that in places a heavier atom occupies the boron site. This is especially visible on the [100] image, where the B rows are theoretically parallel to $\vec{a}$ so that the substitution of B by Mn leads to a significant variation of the contrast at the level of the cation position but also of the surrounding oxygen atoms. Two examples are circled in Figs. 7 and 10a assuming that Mn is locally replacing B; the sequence of the cations along $\vec{c}$, in the mixed chain, is B–Mn–Mn–Mn, as drawn in Fig. 10b. However, the problem of such a substitution is the extent of the defect along the direction of observation. Theoretically, the additional Mn atom is placed in a row of borate groups running along $\vec{a}$ (Fig. 10c). An ideal substitution requires the introduction of two corner-sharing MnO_5 pyramids to respect the Mn and B coordinations. The representation of the polyhedra stacked along $\vec{a}$ at the level of the defect is given in Fig. 10c. Another point is the nature of the coordination polyhedra surrounding the substituting Mn. The substitution of B by Mn implies the presence of

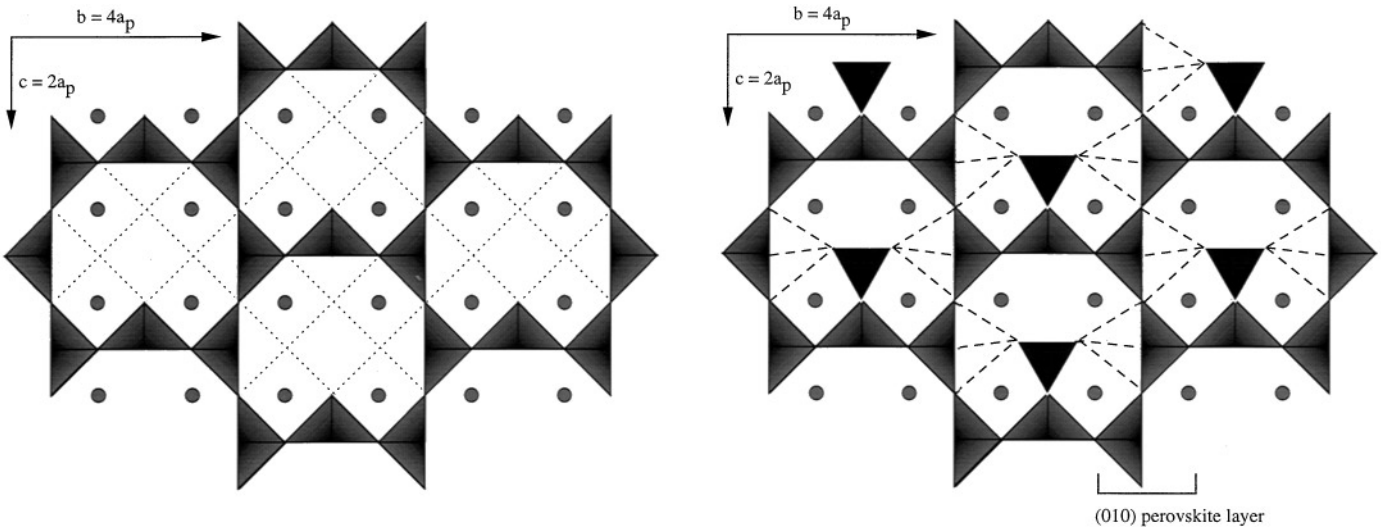

FIG. 8. $Sr_4Mn_3BO_{10}$: [100] projection of the structure showing the mode of connection of the borate groups (dark triangles) and the MnO_5 pyramids. The dotted lines are drawn to illustrate the distorted character of the MnO_6 octahedra, which can be interpreted by the presence of pyramids and "free apices" for the borate groups.

additional oxygen atoms in the (100) layer to ensure a normal coordination for Mn. This change does not involve necessarily the formation of octahedra but can be explained, here again, by the existence of pairs of pyramids if the oxygen vacancies are located along [100].

In a general way, viewed along [100], these defects are isolated so that, in the thicker parts of the crystallites, the intensity of the dots is averaged and one observes regular images (as Figs. 3 and 7). That means also that the extent of the defect along $\vec{a}$ is short. For a few grains, we observed, however, a speckled contrast as observed in Fig. 10a, where the boron positions appear as more or less bright dots. The variation of contrast is correlated with the local substitution of boron groups by manganese pyramids, this substitution running along several unit cells along $\vec{a}$. The simulated images calculated for such a feature confirmed this hypothesis.

(*ii*) *short-range ordering*. In some parts of the crystals, short-range ordering phenomena are observed which sometimes induce the existence of extra reflections in the ED patterns, often in incommensurate positions. One example is shown in Fig. 11, where the satellites are in incommensurate positions with $\vec{q}^* \approx 0.57\vec{c}^*$; the intense reflections and satellites are indexed using four indices.

These areas of nonstoichiometry are observed not only in the form of very small areas but also in the form of (0*kl*) slices. A first example is observed in the right part of the image displayed in Fig. 12a. Referring to the bright contrast of the borate groups, a slice parallel to (011) is observed where the boron atoms are replaced by manganese. However, when looking to the perfect structures, on each side of the defective slice, it appears that one domain is translated by $\vec{t} = \frac{1}{2}\vec{c} + \frac{1}{4}\vec{b}$ with regard to the other so that one (0 1 0) [MnO_2] layer is facing one (010) mixed "B/Mn" layer (Fig. 12b).

As shown in the preceding examples, the substitution of one borate group by a MnO_5 pyramid is, by far, the most frequent origin of nonstoichiometry in this material. In a few cases, two adjacent borate groups along $\vec{c}$ are observed in the mixed layers. One example is given in the left part of Fig. 12a. The sequence within the mixed pyramid–borate layer is "B–B–Mn" along $\vec{b}$. In the adjacent mixed layer, the defect is shifted by $\vec{t} = \vec{c} + \frac{1}{2}\vec{b}$ (Fig. 12c) so that the defect is propagated in a plane parallel to (031).

These HREM observations demonstrate, in agreement with the XRD and EDS results, that manganese replaces partially boron mainly in an homogeneous way. They support strongly the fact that additional manganese exhibits a pyramidal coordination, so that no oxygen excess is needed due to the Mn for B substitution. Finally, it is remarkable that the variation of Mn and B distribution appears in the form of an isolated defect; i.e., no boron free area was observed. Moreover, the substitution of MnO_5 pyramids for BO_3 groups always occurs along $\vec{c}$ this is in favor of the orientation of the BO_3 groups proposed in the first section.

Magnetic Properties

The inverse molar magnetic susceptibility as a function of temperature is plotted in Fig. 13. The plot reveals an antiferromagnetic behavior with $T_N \approx 240$ K and, at a temper-

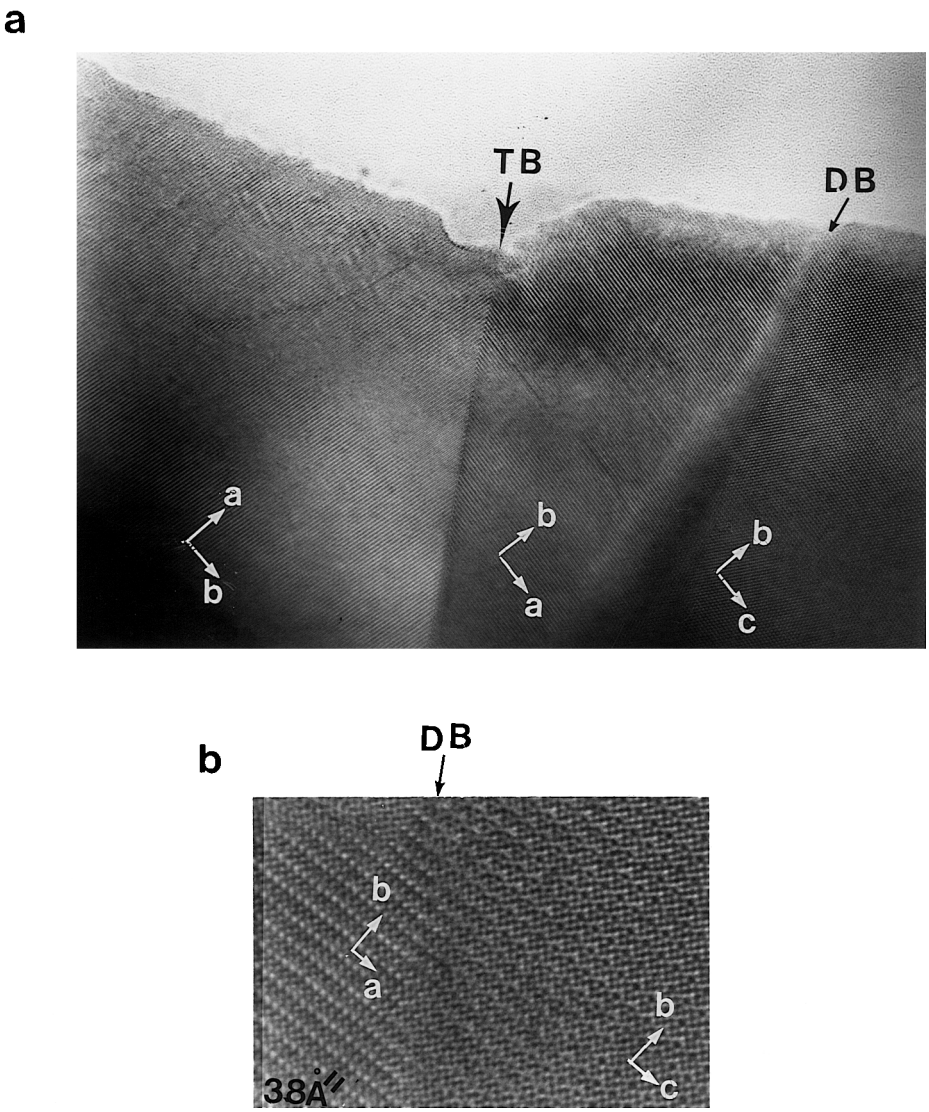

FIG. 9. (a) Overall [100] image of three adjacent domains. From left to right: two twinning [001] domains (the twin boundary is denoted TB) and [100] domain. (b) Enlargement of the non planar domain boundary (DB) separating the [001] and [100] domains. Through the boundary, pure pyramidal (010) layers are connected together. (c) Illustration of a layer connection mode through the domain boundary (DB); the polyhedra are schematically drawn.

ature lower than 160 K, the appearance of ferromagnetic coupling. At high temperature ($T > 400$ K), a paramagnetic behavior is observed. The linear part fitted with a Curie–Weiss law leads to a negative paramagnetic temperature $\Phi_p = -250$ K characteristic of antiferromagnetism. The manganese effective moment $\mu_{eff} = 5.10\ \mu_B$, deduced from the Curie constant considering 3.2 Mn per unit formula, is close to the theoretical value for Mn^{3+} ($\mu_{eff} = 4.9\ \mu_B$). This magnetic behavior is close to that reported for the oxycarbonate $Sr_5Mn_4(CO_3)O_{10}$, which exhibits a Neel temperature of 260 K and an effective moment per manganese $\mu_{eff} = 5.09\ \mu_B$ (4).

CONCLUSION

A new oxyborate $Sr_4Mn_{3.2}B_{0.8}O_{10}$ has been isolated, which results from the ordered substitution of one [100] row of MnO_6 octahedra by one row of BO_3 groups in an ideal perovskite structure. The XRD study showed that it results in a pyramidal framework $Sr_4Mn_3O_8$, forming large tunnels parallel to the [100] direction occupied by the triangular BO_3 groups. The manganese excess with regard to the ideal formulation $Sr_4Mn_3BO_{10}$ is accommodated through a statistical substitution of Mn for B. The different nanostructural mechanisms which govern this non-

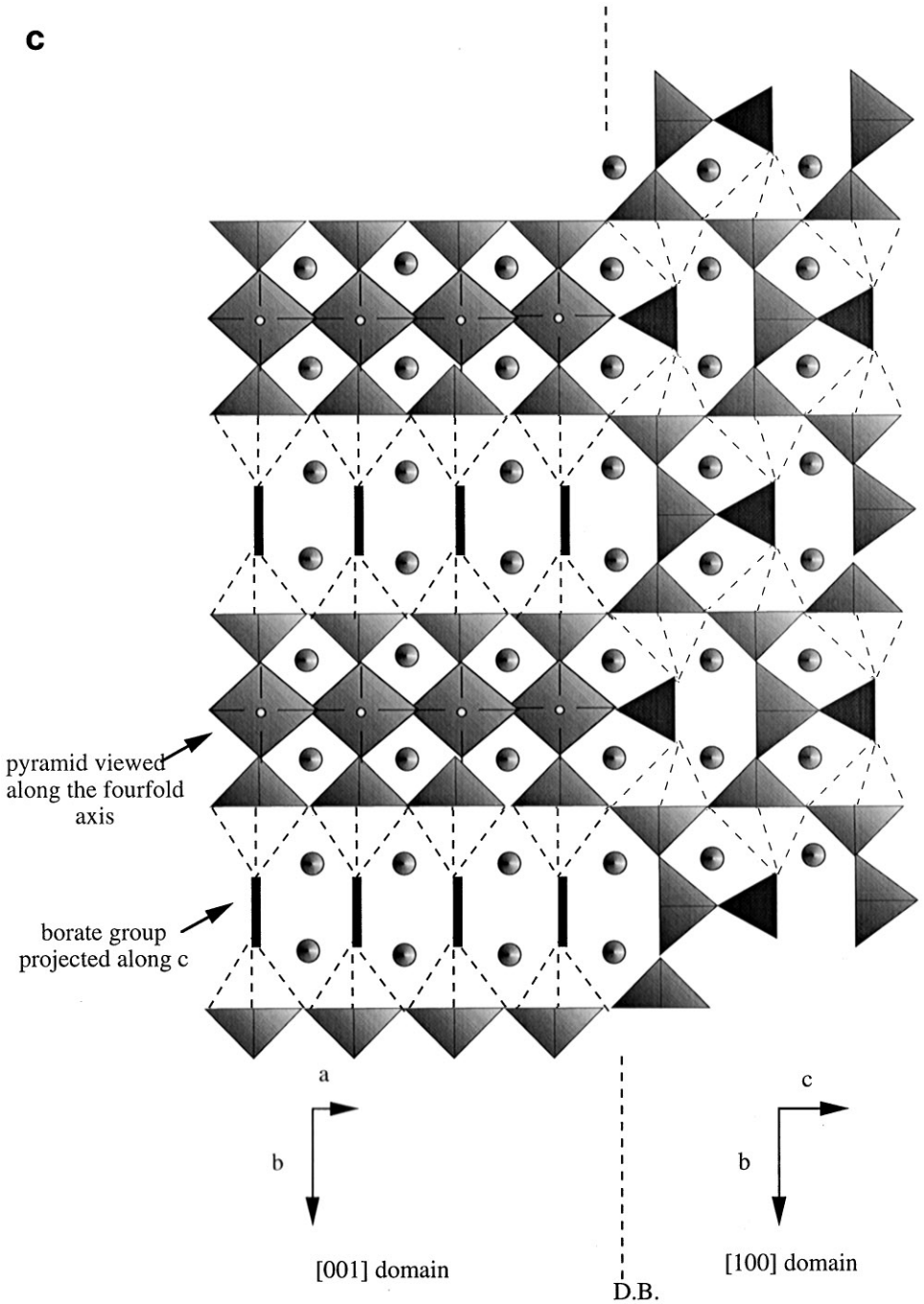

FIG. 9—*Continued*

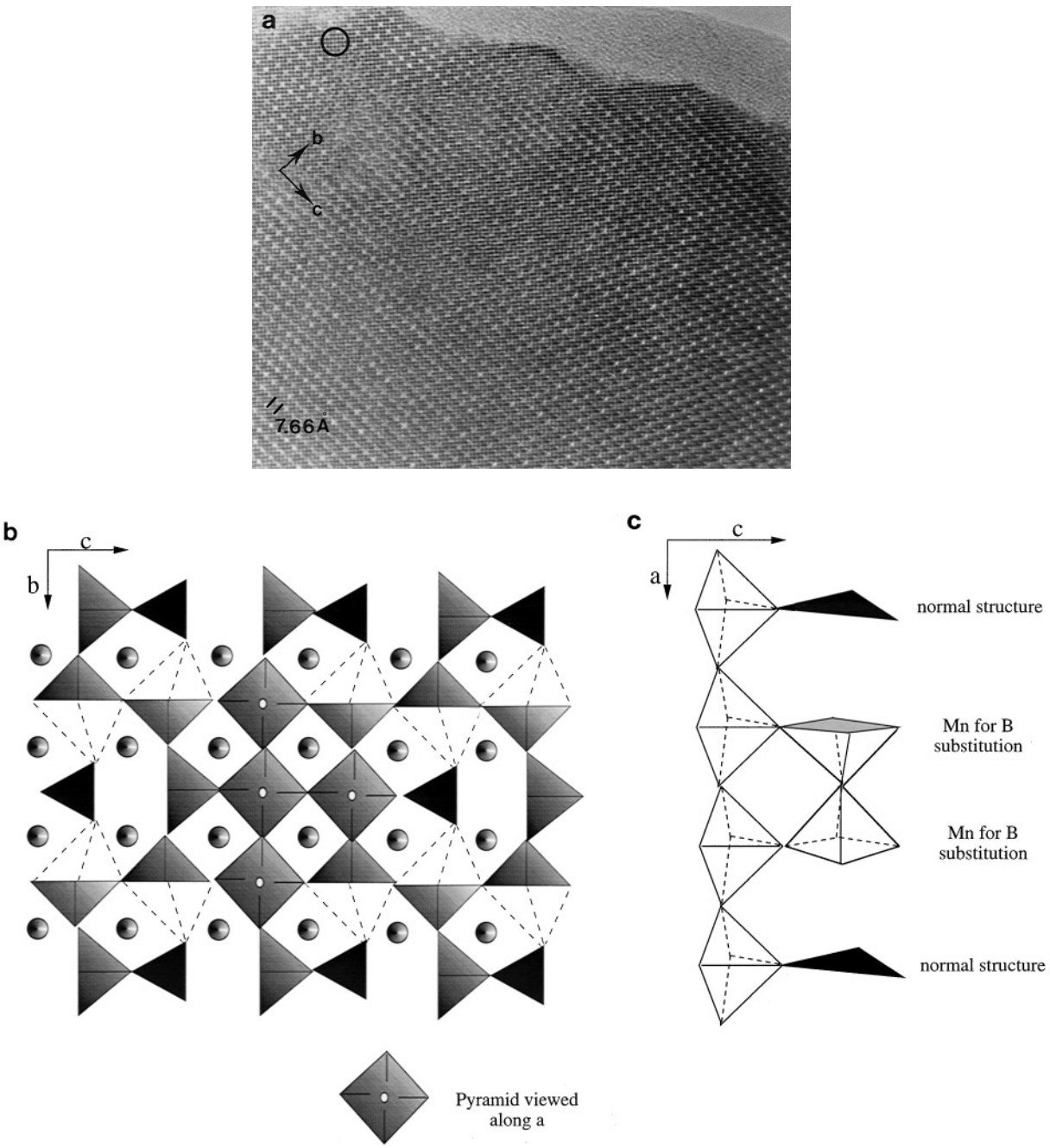

FIG. 10. (a) [100] HREM image of a crystal area where, in an unusual way, the contrast observed at the level of the boron positions is uneven, leading to a speckled aspect of the image. (b) Idealized drawing, projected along [100], of a local manganese for boron substitution. (c) Perspective view, showing the sequence of the polyhedra along $\vec{a}$.

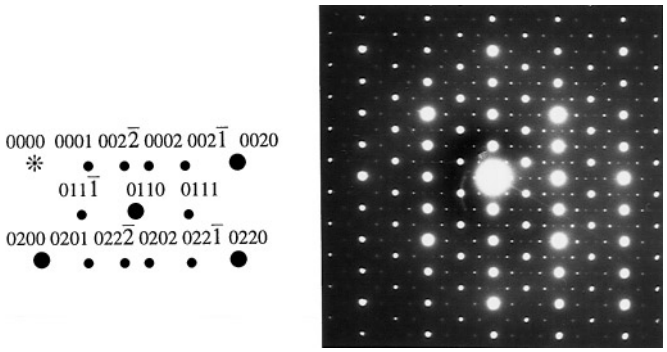

FIG. 11. Experimental [100] SAED pattern of a modulated area, with $\vec{q}^* \approx 0.57\vec{c}^*$ and indexation of the satellites (using four indices).

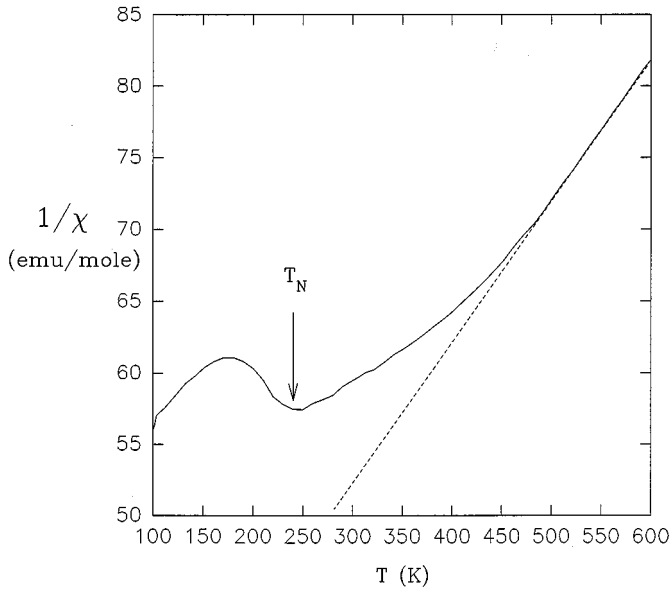

FIG. 13. Inverse molar magnetic susceptibility as a function of temperature.

stoichiometry can be described on the basis of models involving only MnO_5 pyramids and, therefore, retaining the oxygen content, i.e., the valence III for Mn. This is in agreement with the magnetic properties of the oxyborate.

The existence of modulated superstructures, associated with different Mn/B ratios, suggests that other ordering

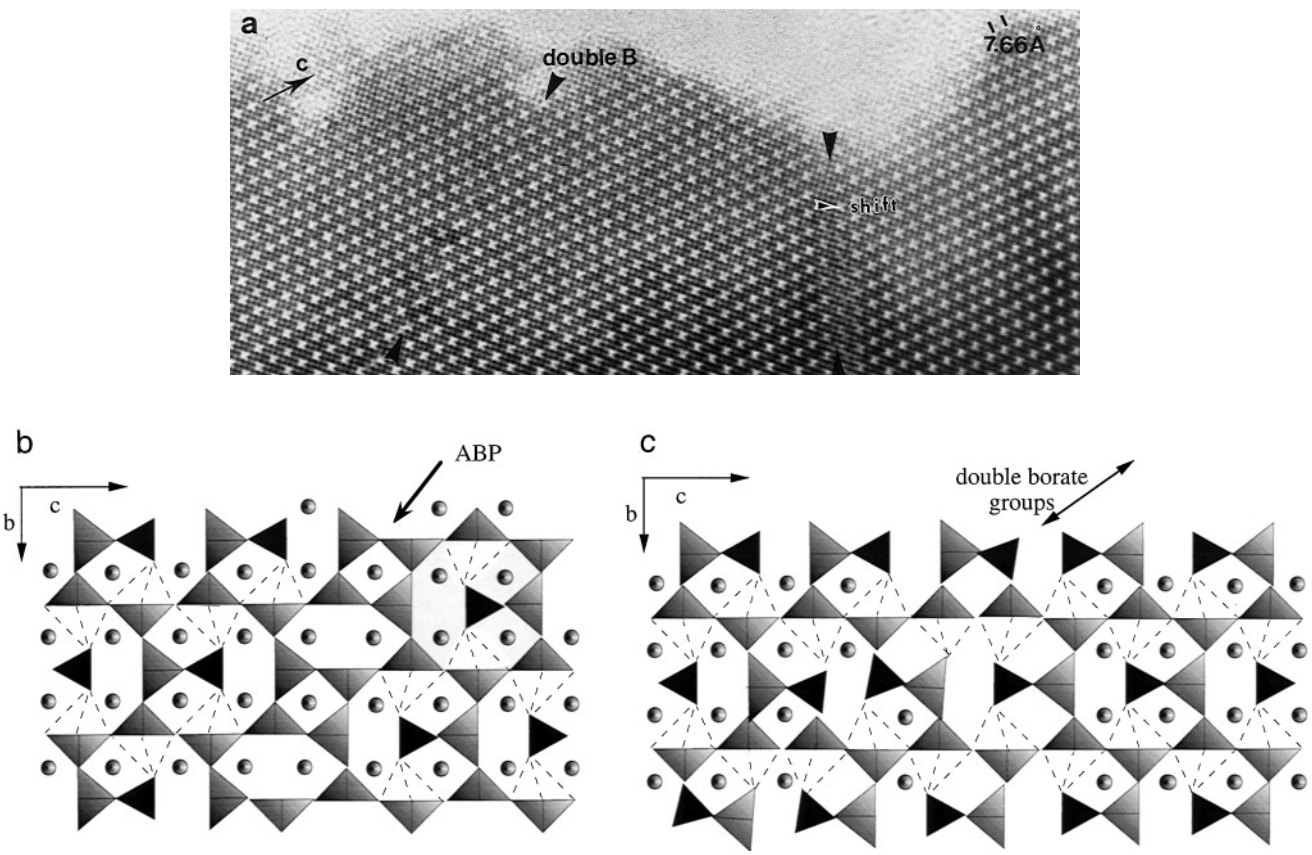

FIG. 12. (a) Two mechanisms of nonstoichiometry are observed in this [100] HREM image: pyramidal "Mn" layers are connected to mixed "Mn/B" (idealized model in (b)) through a defective slice parallel to (011) (the shifting is indicated by a white arrowhead) and double borate groups are arranged in a (031) defective slice (idealized model in (c)).

modes could be stabilized and opens the road to a new family of materials.

REFERENCES

1. B. Raveau, C. Michel, and M. Hervieu, *C. R. Acad. Sci.* **322,** 609 (1996); B. Raveau, C. Michel, M. Hervieu, and A. Maignan, *J. Mater. Chem.* **5,** 803 (1995).
2. T. Kawashima, Y. Matsui, and E. Takayama-Muromachi, *Physica C* **224,** 69 (1994); M. Alario-Franco, P. Bordet, J. J. Capponi, C. Chaillout, J. Chenavas, T. Fournier, M. Marezio, B. Souletie, J. Sulpice, J. L. Tholence, C. Colliex, M. F. Gorius, and M. Peroux, *Physica C* **231,** 103 (1994); J. L. Allen, B. Mercey, W. Prellier, J. F. Hamet, M. Hervieu, and B. Raveau, *Physica C* **241,** 158 (1995).
3. Li Rukang, R. K. Kremer, and J. Maier, *J. Solid State Chem.* **105,** 609 (1993); R. Norrestam, M. Kritikos, and A. Sjödin, *Acta Crystallogr., B* **50,** 631 (1994).
4. V. Caignaert, B. Domenges, and B. Raveau, *J. Solid State Chem.* **120,** 279 (1995).
5. J. Rodriguez-Carvajal, "Powder Diffraction Satellite Meeting of the XVth Conference of the International Union of Crystallography, Toulouse, France." Abstracts, p. 127, 1990.
6. B. Domenges, M. Hervieu, and B. Raveau, *Physica C* **207,** 65 (1993).
7. Ph. Boullay, B. Domenges, M. Hervieu, and B. Raveau, *Chem. Mater.* **5,** 1683 (1993).
8. A. Reller, J. M. Thomas, D. A. Jefferson, and M. K. Uppal, *Proc. R. Soc. London, A* **394,** 223 (1984); K. R. Poeppelmeier, M. E. Leonowicz, J. M. Longo, and W. B. Yelon, *J. Solid State Chem.* **45,** 71 (1982).
9. V. Caignaert, *J. Magn. Magn. Mater.* **166,** 117 (1996).